JOURNAL OF MATERIALS RESEARCH AND TECHNOLOGY 2023;25:2455–2470

Available online at www.sciencedirect.com

jmr&t Journal of Materials Research and Technology

journal homepage: www.elsevier.com/locate/jmrt

The effects of pressure and pressure routes on the microstructural evolution and mechanical properties of sintered copper via SPS

Francisco Briones [a,b,*], *Vanessa Seriacopi* [a,c], *Carola Martínez* [d], *José Luis Valin* [b], *Dany Centeno* [e], *Izabel Fernanda Machado* [a]

[a] *Departamento de Engenharia Mecatrônica e Sistemas Mecânicos, Escola Politécnica, Universidade de São Paulo, Av. Prof. Mello Moraes 2231, São Paulo, 05508–030, SP, Brazil*

[b] *Escuela de Ingeniería Mecánica, Pontificia Universidad Católica de Valparaíso, Los Carrera, Quilpué, 01567, Chile*

[c] *Departamento de Engenharia Mecânica, Instituto Mauá de Tecnologia, Praça Mauá 01, São Caetano Do Sul, 09580-900, Brazil*

[d] *Departamento de Ingeniería de Obras Civiles, Universidad de La Frontera, Francisco Salazar, Temuco, 01145, Chile*

[e] *Departamento de Engenharia Metalúrgica e de Materiais, Escola Politécnica da Universidade de São Paulo, Av. Prof. Mello Moraes 2463, São Paulo, 05508-030, SP, Brazil*

ARTICLE INFO

Article history:
Received 3 January 2023
Accepted 11 June 2023
Available online 14 June 2023

Keywords:
Copper
SPS
Microstructure
Pressure application route influence

ABSTRACT

Spark Plasma Sintering (SPS) is a pressure-assisted sintering process in which high density and mechanical properties are usually reached. This study applied the SPS to consolidate copper powder using different sintering pressures and pressure routes during holding time or heating. In the first route, the pressure was maintained (around 15 MPa) during the heating up to the sintering temperature (650 °C), and the pressure was increased during the holding time. In the second route, the pressure was raised during the heating and kept constant during holding time at 650 °C. Three different pressure levels were applied on each route: 110, 65, and 50 MPa. Microstructural evolution was investigated using densification (Archimedes method), scanning electron microscopy (SEM), hardness, and X-ray diffraction (XRD). The increase in pressure improves the microstructural features. In addition, in the first route, in which higher pressure rates were found, grain growth inhibition was observed, and densification was also improved significantly. The smallest crystallite size and highest microstrain were also observed at higher pressures. The increase in pressure also led to a rise in microhardness (17%), a decrease in pore volume fraction (10.5%), and an increase in pore circularity, causing substantial variations between the microstructures of samples. A finite element method (FEM) analysis was conducted using a thermo-mechanical approach to evaluate the stress distribution in the two different sintering routes. The results agree with the experimental results, and more pronounced effects were found in the first route because of higher compressive stresses, corroborating the results of microstrain and hardness.

* Corresponding author. Escuela de Ingeniería Mecánica, Pontificia Universidad Católica de Valparaíso, Los Carrera, Quilpué, 01567, Chile

E-mail address: francisco.briones@pucv.cl (F. Briones).

https://doi.org/10.1016/j.jmrt.2023.06.099

1. Introduction

Copper is widely used in different applications due to its excellent electrical and thermal conductivity, corrosion resistance, and tribological behavior. Therefore, this element is one of the most common materials used in mechanical and electrical systems, such as friction plates [1], brake pads [2], and electronic contact devices [3]. However, the low hardness and mechanical strength may restrict the performance of copper-made components. Performance improvement has been aimed at using copper manufacturing at micro and nanometric scales employing processes such as electron beam melting [4], microwave [5], and conventional sintering [6]. However, achieving a significant increase in microhardness (>60 HV) and effectively inhibiting grain growth without optimizing manufacturing processes is challenging.

Powder metallurgy (PM) is a large-scale manufacturing, and it is one of the most widely used methods to obtain copper-based materials [7,8]. One of the steps of PM is the sintering, which usually is carried out below the melting point of metallic, ceramic, or composite material. The densification occurs due to the decrease the surface energy as well as grain growth. However, as mentioned above, the mechanical properties may be limited due to excessive grain growth during sintering. As a practical alternative, Spark Plasma Sintering (SPS) has been proposed as a successful process that allows a strengthening mechanism due to the low residual pore volume fraction (densification). The SPS performance is achieved due to high heating rates (10–1000 °C/min), shorter holding times, and full densification in a few minutes at lower temperatures than conventional sintering techniques. Therefore, grain growth is hindered. It is well-known that SPS is an advanced processing technology to produce homogenous, highly dense, nano-structural sintered compact, composite materials, functionally graded materials (FGMs), fine ceramics, wear-resistant materials, thermoelectric semiconductors, and biomaterials. Furthermore, it is a versatile technique for fabricating copper-based materials with high reproducibility and significantly reducing the total duration of the process [9]. In comparison to other sintering techniques, such as Hot Pressing (HP), Hot Isostatic Pressing (HIP), and Microwave Sintering (SM), SPS reduces sintering temperature and dwell times due to pressure - assisted system during sintering. In addition, it provides a better combination of microstructural characteristics, improving mechanical and tribological performance [10–13].

Concerning the heating rate, the sintering temperature, and the pressure, SPSed samples have been the subject of extensive research. In general, sintering temperatures of metallic materials, ranging between 600 and 1100 °C and pressures between 15 and 80 MPa (constant pressures during holding time) are adequate to effectively produce an material almost entirely dense material [14–16]. For instance, due to the short holding times and high heating rates, copper nanoparticles were sintered via SPS to obtain fine-grained materials. Studies exploring the use of SPS to consolidate ultrafine powdered copper (1 μm) showed 99% densification, 350 MPa of tensile strength, and 56% elongation at the sintering temperature of 750 °C due to grain size refinement [17,18]. R. Ritasalo et al. [19] sintered nanometric copper particles (50 nm) at temperatures ranging from 600 to 800 °C and reached densities greater than 97%, hardness varying between 1.26 and 1.10 GPa, and yield stress between 413 and 313 MPa, respectively. K. N. Zhu et al. [20] found SPSed copper (average particle size of 520 nm) densities above 98% and grain sizes varying from 0.62 to 4.11 μm. The samples were sintered at temperatures ranging between 800 and 1000 °C, the pressure of 50 MPa, and holding times of 5 min. Although the grain size increased with the sintered temperature, it remained small.

Other works have shown that the SPS mechanical pressure-assisted system is beneficial in achieving theoretical density in metallic materials [21,22]. For example, Z. H. Zhang et al. [23] sintered copper powder (1 μm) at 800 °C, varying the pressure from 0 to 50 MPa, and considering the holding time of 6 min. The authors observed that the initial sintering pressure of 1 MPa up to a maximum pressure of 50 MPa during the holding time considerably increased the relative density from 74 to 98%, and, although not significantly, hindered grain growth (from 6.4 to 5.6 μm at the highest pressure). In addition, the relationship between the relative densities and the holding between 3 and 15 min, at a constant pressure of 50 MPa, showed a lower effect, and the difference in the relative density varied from 96.76% to 98.71%, respectively. It is worth noticing that the maximum pressure applied must be higher than 25 MPa.

Pressure and temperature during sintering are the most studied parameters to obtain optimized results using the SPS technique. The advantage of applying high pressure is to uniformly distribute stresses and improve the contact points between particles within the sintered sample, inhibit grain growth and achieve high densification, as has already been shown in the literature [24–26].

It is worth mentioning that the influence of sintering parameters on the characteristics of sintered copper via SPS previously mentioned was presented in several studies [14,17,23,27–31]. However, copper powder SPSed with different pressure routes and high pressures (above 50 MPa) has not been reported yet. Therefore, understanding the influence of varying sintering parameters (pressures and the pressure routes) applied during holding time and heating on the evolution of porosity, grain growth, and mechanical properties of copper sintered by SPS remains a challenging subject of interest. In addition, a finite element method FEM approach with experimental validation was carried out to achieve this objective, considering sintering models to show the stress distribution during the sintering routes.

2. Experimental and numerical procedures

2.1. *Material and sintering parameters*

This study used commercial atomized copper powder (Sigma Aldrich, 99.9% purity, <75 μm) as raw material.

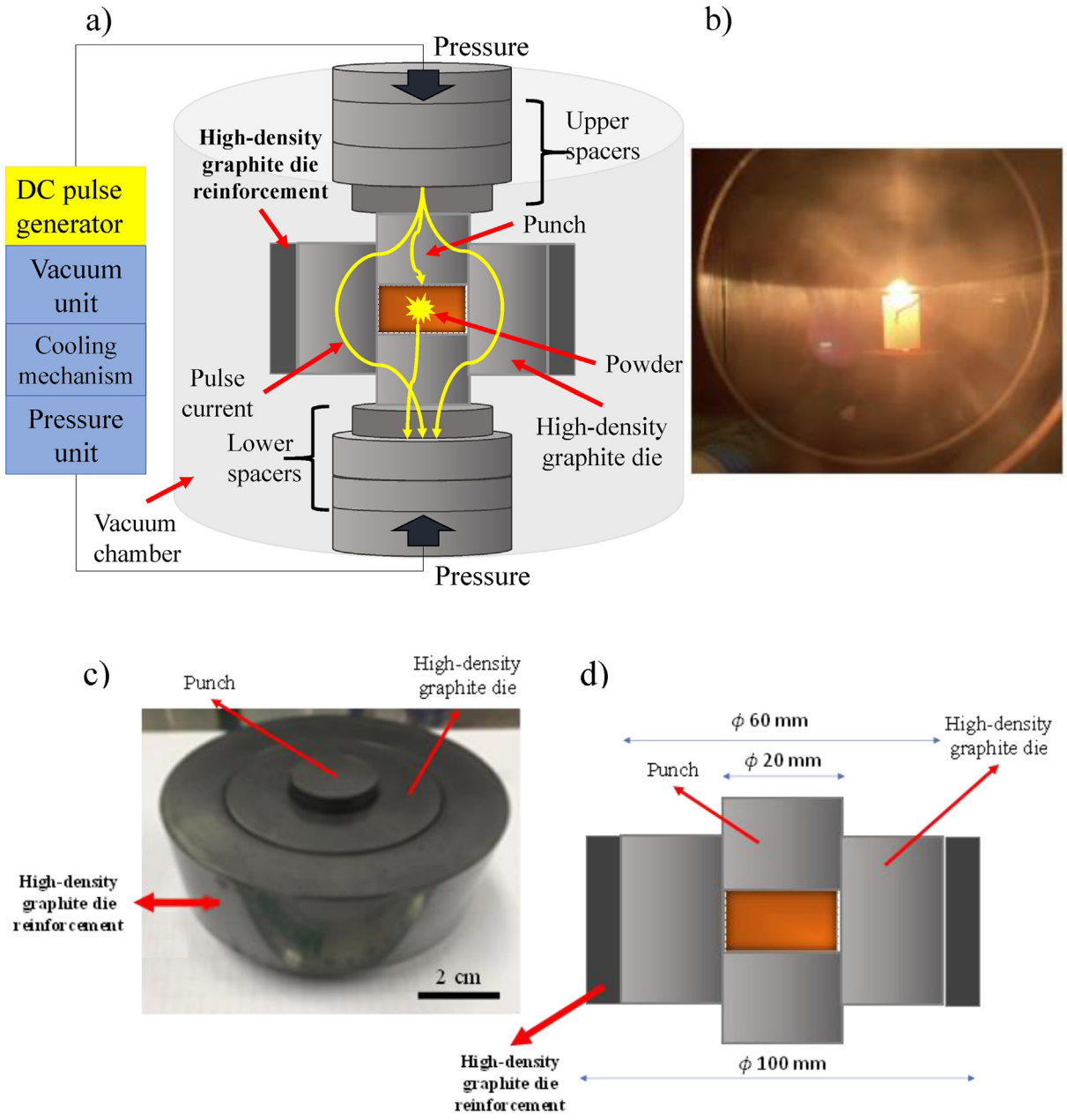

Fig. 1 – a) Schematic representation of the SPS system, b) the die and graphite punches during copper sintering at 650 °C inside the SPS vacuum chamber, c) high-density graphite die assembly and d) high-density graphite die dimensions.

The SPS device, model DR. SINTER® SPS1050 (Fuji Electronic Industrial Co), was used to sinter the copper powder samples. Copper powder (approximately 15 g) was placed in a high-density graphite die, similar to that used in other works [12]. The samples were 20 mm in diameter and 5 mm in thickness (discs). The die had 60 mm in external diameter, 20 mm in internal diameter, and 40 mm in height. Two high-density graphite punches were used (cylinders of 20 mm in diameter and 20 mm in height). The powder was placed between the punches. Therefore, the die setup was placed inside another external graphite die to improve the toughness of the systems and allow higher pressure application. Fig. 1 shows a schematic of the sample assembly.

The samples were heated from room temperature to 650 °C, and the holding time was 2 min, a low vacuum of about 20 Pa was maintained during the sintering.

An axial pressure was applied during sintering using two different routes. In the first route, the pressure was maintained at 15 MPa during the heating up to the sintering temperature at 650 °C; then the pressure was increased during the holding time. This route was denominated HT. In the second route, the pressure was raised during the heating and kept

constant during holding time at 650 °C. This route was denominated H. Three different pressure levels were applied on each route: 110, 65, and 50 MPa. Each route and maximum pressure used are displayed in Table 1.

Table 1 also summarizes the sintering parameters and sample denomination used in this work. Fig. 2 displays a schematic of the heating and pressure applied described in Table 1.

2.2. Material characterization

The copper particle size distribution was determined using a laser scattering particle analyzer (Hydro 2000-UM).

The densification of the samples was evaluated to verify the influence of different pressures and pressure routes (HT and H) on the relative density. It was determined according to the Archimedes method described elsewhere [32].

Copper samples after sintering were also metallographically prepared following a usual procedure. The samples were embedded and mechanically ground using 600–1200 meshes of SiC paper. The polishing of the sintered materials was carried out in two steps: i) first, a diamond suspension with a particle size of 6, 3, and 1 μm was utilized, and ii) second, a colloidal silica suspension for the final finishing with a particle size of 0.04 μm. All samples were immersion-etched with ferric chloride III ($FeCl_3$) reagent for 7 s. Finally, to eliminate any particles on the surfaces, samples were immersed in alcohol (ultrasonic bath). After cleaning, samples were dried and observed using an optical microscope (Olympus BX60 M) to evaluate their cleanliness.

The microstructure was observed using scanning electron microscopy (SEM) JEOL-JSM 6010LA, Field emission microscopy FEI-Inspect F50 (FESEM) equipped with the energy dispersive analysis (EDS), and backscattered electrons (BSE). The size and shape of pores for each sample were quantitatively analyzed based on several sets of SEM-FESEM images by counting at least 290 grains at different magnifications. Samples were observed without etching, avoiding pore boundary etching. The evaluation of the pore features was carried out using tools such as grayscale (RGB image conversion to 8 bits), segmentation by a threshold, and automatic conversion of images to binary images obtained using Image J® software. Furthermore, SEM micrographs showed a strong contrast between pores and the copper matrix. The software made it possible to analyze the circularity index (Ci) parameters and the shape factor. The shape factor exhibits values between 0 and 1; values closer to 1 indicate circular pores, while values closer to zero indicate irregular shape pores. The size of the pores (S_p) was also determined. C_i and S_p were calculated using equations (1) and (2), respectively [33,34].

$$C_i = \frac{4\pi A_p}{P_p^{\,2}} \tag{1}$$

$$S_p = \left(\frac{A_p}{\pi}\right)^{\frac{1}{2}} \tag{2}$$

where A_p is the pore area, and P_p is the pore perimeter.

The Analysis of Variance (ANOVA) through a Tukey test was used to evaluate the statistical significance of the grain size determination for the different sintered samples, considering a significance level (p) corresponding to 5%.

Microhardness measurements were carried out to determine the effect of sintering pressure parameters. It was assessed using Vickers microhardness tests (MMT-3 micro durometer from Buehler). At least ten indentations were performed by applying a static load of 10, 50, and 100 gf for 10 s at room temperature, following the procedure described elsewhere [35].

X-ray diffraction (XRD) measurements were carried out to identify the crystalline phases in the samples using an Empyrean 3rd generation Malvern Panalytical diffractometer using Cu-Kα radiation (λ = 1542 Å and 2.2 kW). Sample preparation was the same as described above to avoid surface damage. XRD data was recorded in conventional Bragg-Brentano geometry for 2θ scans ranging from 20 to 100° with a step of 0.02° and a step count time of 2 s/step. A current of 20 mA and a voltage of 40 kV were used as settings. The crystalline phases present in the XRD patterns were determined using MATCH! 3 software version 3.14 equipped with the Crystallography Open Database (COD). A pseudo-Voigt function generated the line shape of the diffraction peaks. Crystallite size and microstrain were determined via the traditional Williamson-Hall method. This method considers that peak broadening is produced by crystallite size and isotropic microstrain variations [36].

2.3. Finite element analysis

The three-dimensional (3D) modeling using the Finite Elements Method (FEM) was simulated based on the sintering process parameter using Abaqus/Standard® software. The FEM approach model considered a coupled thermo-mechanical evaluation and homogeneous microstructures to assess the influence of the pressure rate application route in the 25HT-65 MPa and 7.1H-65 MPa samples (see Table 1 and Fig. 2) on the stresses related to the sintering process [37]. The effect of the rigid graphite die was considered using

Table 1 – Maximum pressure, pressure rate on the different routes, and terminology assigned to the copper samples.

Samples	Maximum pressure achieved (MPa)	Pressure rate applied during the holding time (**HT**) (MPa min^{-1})	Pressure rate applied during the heating (**H**) (MPa min^{-1})
47.5HT-110 MPa	110	47.5	-
13.6H-110 MPa	110	–	13.6
25HT-65 MPa	65	25	-
7.1H-65 MPa	65	–	7.1
17.5HT-50 MPa	50	17.5	-
5H-50 MPa	50	–	5.0

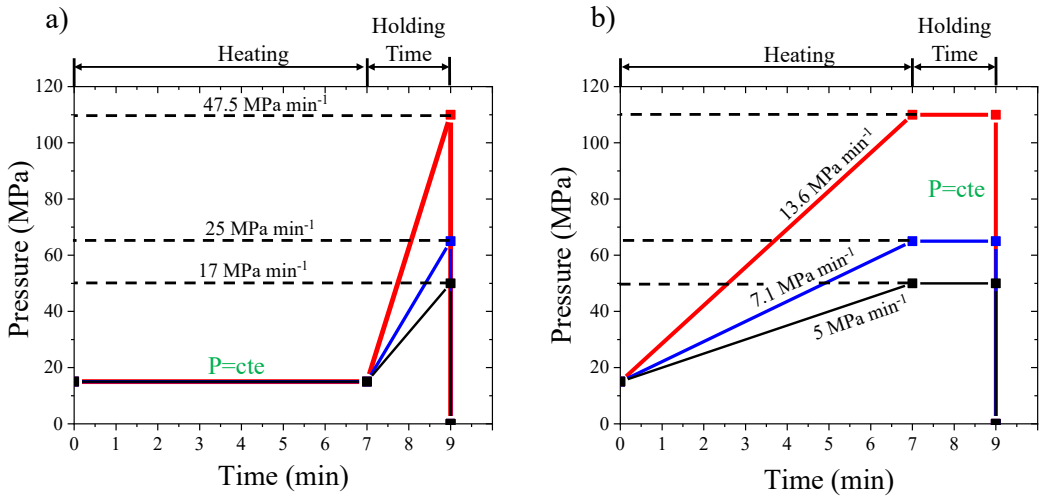

Fig. 2 – Pressure routes: a) pressure rates during holding time (HT) – First route, b) pressure rates during heating (H) – Second route.

mechanical constraints, and the sintering pressure uniaxial was applied on the upper surface of the samples. The dimensions and geometry of the simulated samples were 20 mm in diameter and 5 mm in thickness. The two sintering pressure routes were taken into account, in which the outputs were mainly analyzed in two stages: (i) end of the heating (420 s); and (ii) end of holding time (540 s). The geometry of the samples was discretized into a mesh with a spatial resolution of 1 μm, totaling 100,800 deformation elements and 110,891 nodes. Fig. 3 presents the general geometry, boundary conditions, and uniaxial loads.

However, sintering models can involve high complexity and computational resources based on multiphysics analyses. In the present work, some simplified hypotheses were taken into account to assess stress fields resulting from the sintering process of the samples. Previous studies of this thermo-mechanical approach [38] correlated well with experimental results, validating the methodology developed. The following simplifications were considered herein.

(i) the sintered workpiece was considered deformable, and the dies were assumed rigid. In conclusion, the finite

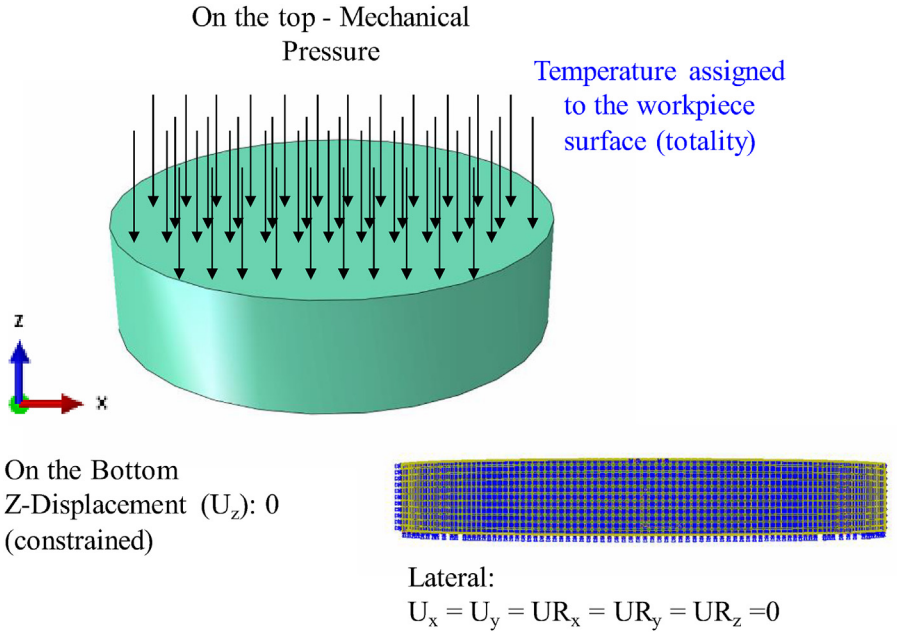

Fig. 3 – Discretization of the mesh of the sample geometry. Model the geometry along with the displacement boundary conditions and loads on the upper surface of the sample.

Table 2 – Mechanical and thermal properties of the copper samples [38–41].

Mechanical Properties						
Density [kg m^{-3}]	Elastic Modulus [GPa]	Poisson Ratio	Yield Stress [MPa]	Ultimate Tensile Stress [MPa]	Elongation at break [%]	Inelastic Heat Fraction
8960	120 (25 °C)	0.36	333.4 (25 °C)	344	14	0.9
	83 (650 °C)		98.0 (650 °C)	–	–	
Thermal Properties						
Temperature [°C]	Thermal Conductivity [$Wm^{-1}K^{-1}$]	Thermal expansion coefficient [$\mu m\ m^{-1}K^{-1}$]		Specific heat [$Jkg^{-1}{}^{\circ}C^{-1}$]		
27	398	16.4		385		
727	357	24.8				

element mesh was focused and assigned only to the workpiece;

(ii) mechanical (pressure and distinct routes) and thermal (temperature and variable amplitudes) loadings were inserted into the model because of the experimental SPS process conducted. Therefore, the electrical and thermal effects during this sintering can be indirectly incorporated using normal mechanical pressures and temperature fields. The approach helps to converge the numerical model, providing the reproduction of experimental parameters that can be measured;

(iii) in addition, constraints and boundary conditions were imposed according to Fig. 3 to consider the spatial movement restrictions due to the SPS system with the dies and punches. Since the focus consisted of the workpiece, a friction coefficient was not used as a model input.

The thermo-mechanical model during the holding time considered thermal properties (i.e., thermal conductivity, specific heat) and mechanical properties (i.e., Poisson's ratio, elastic modulus, and yield strength) are depicted in Table 2 This model was developed to reproduce the behavior of stresses on the material's surface during the holding time, including the shear stresses. The modeling considered temperature varying from room temperature to the sintering temperature (650 °C). It is worth mentioning that the results intend to complement the analysis based on the pressure rate applied.

3. Results and discussions

3.1. Powder characterization

Fig. 4 a-b) shows the morphology of the copper powder (Sigma Aldrich, 99.9% purity), from which it is possible to observe an irregular morphology of the particles and rounded edges. Agglomerates of particles were also observed. The particle size distribution is shown in Fig. 4 c), from which a monomodal size distribution can be observed. The particle diameters' characteristic equivalents were: $d_{90} = 33.05\ \mu m$, $d_{50} = 17.88\ \mu m$, and $d_{20} = 8.91\ \mu m$.

Fig. 4 d) shows the results of the X-ray diffraction analysis. The copper particles are indexed as α-Cu single phase, and no secondary phases are identified in the X-ray diffraction pattern.

3.2. Microstructural characterization of sintered samples

3.2.1. XRD analysis

Fig. 5 shows the X-ray diffraction patterns of the sintered samples in different sintering conditions (see Table 1 and Fig. 2). Copper diffraction peaks from the XRD analysis indicate the presence of copper oxides (Cu_2O and CuO) in the sintered copper samples. The presence of these oxides could be attributed to the oxidation of copper powder exposed to the environment. However, the XRD patterns revealed that no significant oxidation of the samples occurred, indicating the effectiveness of the SPS sintering process. According to Romaric et al. [9], the presence of oxide on the surface of the particles can delay the sintering mechanisms in cases of a high presence of oxides and low sintering pressures (4 MPa). However, in this study, pressures above 50 MPa and the presence of these oxides in small quantities do not influence the densification, according to reports in the literature [22].

The main objective of this analysis was allowed to compare the effect of the applied pressure and pressure routes based on the crystallite size and microstrain ($<\varepsilon^2>^{1/2}$). The results in Fig. 5 do not show significant differences between the samples. Hence, additional results are displayed in Table 3, which presents the microstructural parameters obtained from the X-ray diffraction patterns using the Williams-Hall method [36].

The pressures applied and pressure rates during sintering influence the crystallite size. The sample sintered at 50 MPa and pressure applied during holding time (HT) showed a double crystallite size of the sample in which 110 MPa was applied. Similar behavior was noticed in samples when pressure was applied during heating. However, the effect of pressure was less pronounced. Regarding the microstrain ($<\varepsilon^2>^{1/2}$), the trend is the opposite of the crystallite size; the higher the applied pressure and pressure used during holding time, the higher the results are. A similar study using nickel showed smaller crystalline sizes and higher microstrain in samples presenting higher hardness [42]. The higher pressures and the rise in the rate of pressure at the highest temperature increase the crystalline defects in the material. This increase was not characterized using microscopy techniques, but XDR is a well-known and exact technique to detect

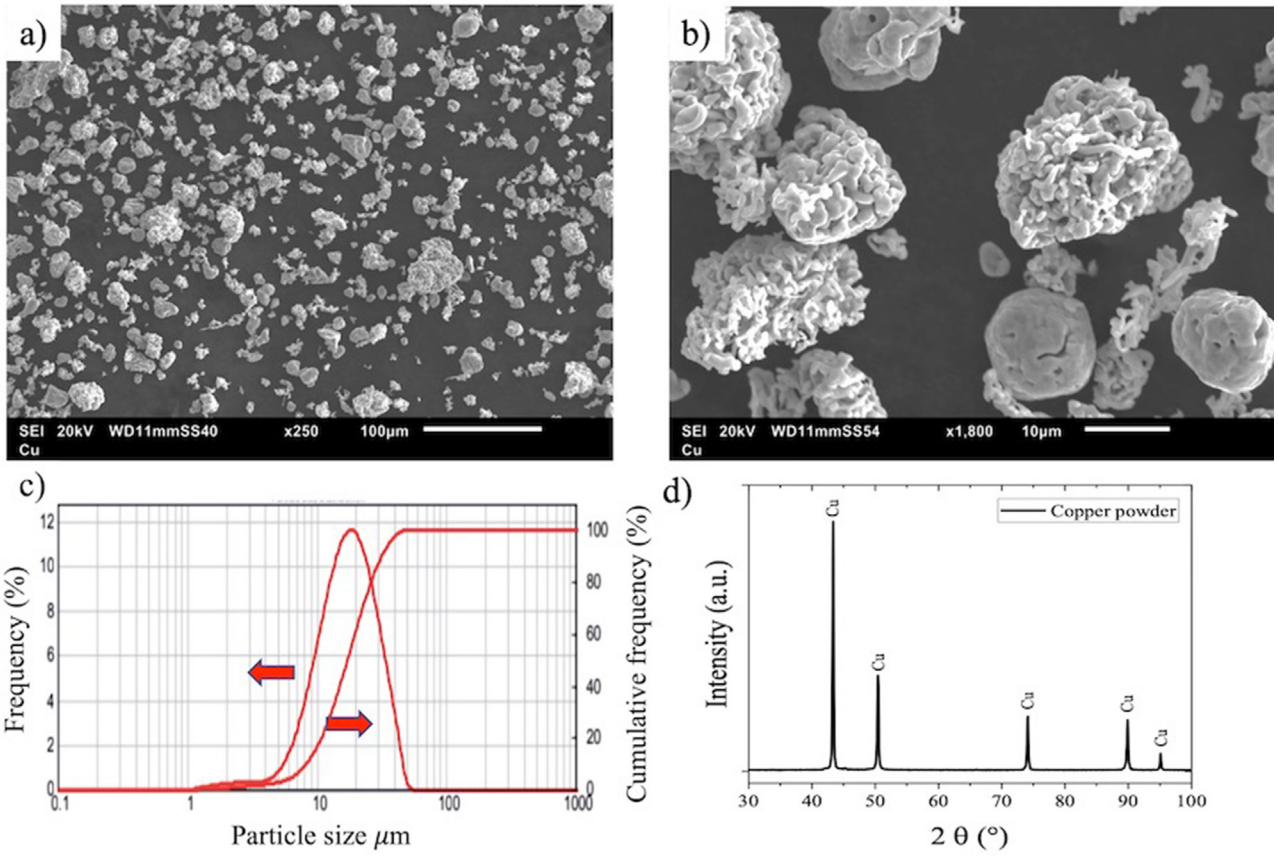

Fig. 4 – (a-b) Images SEM of size and shape of copper particles, (c) copper particle size distribution, and d) copper powder XRD patterns.

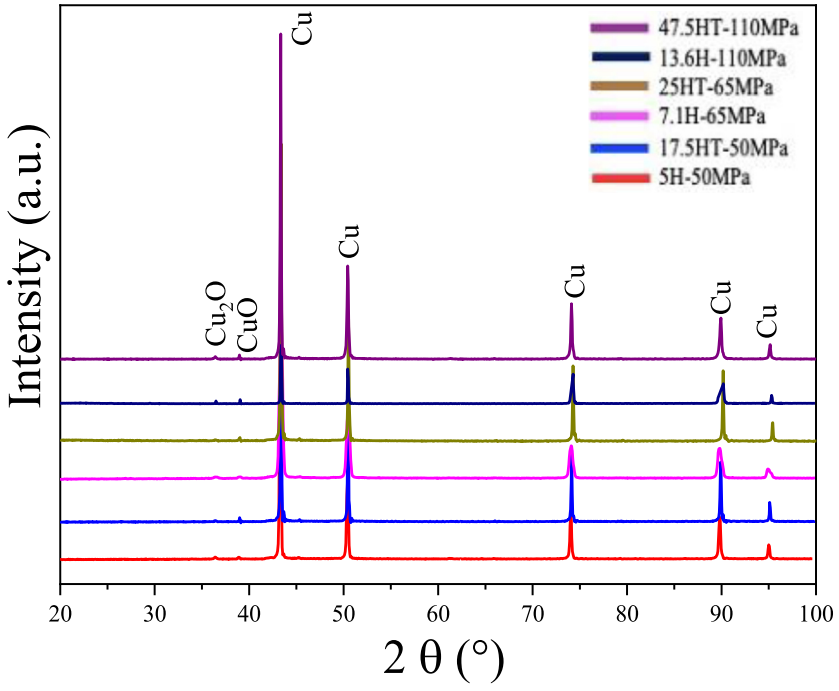

Fig. 5 – Copper XRD diffraction pattern after sintering at different conditions.

alterations in the crystalline structure. Hardness results will be discussed later on, and they will complement this discussion.

Concluding, the increase in pressure, independently of the route of applying pressure, was followed by an increase in the microstrain and caused a decrease in the crystalline size. The HT route, in which the pressure was increased during holding time, at 650 °C, and lower yield strength, caused a more pronounced effect. Therefore, the effects cannot be wholly decoupled, and they are complementary since they are caused by the increase in crystalline defects.

3.2.2. *Densification*

The relative density obtained by the Archimedes method and the porosity measurement using image analysis of sintered samples are shown in Table 4. The results allow observing the contribution of the different pressures and pressure routes, which resulted in a higher density for 47.5HT-110 MPa sample (8.78 g/cm^3) than 17.5HT-50 MPa (7.71 g/cm^3) as well as 13.6H-110 MPa sample (8.60 g/cm^3) compared to 5H-50 MPa one (7.17 g/cm^3).

The densification results (Table 4) obtained indirectly from the Archimedes method and directly from the porosity image analysis. Therefore, samples under pressure during holding time presented an improved relative density. Additionally, there was a significant reduction in the number of large pores.

The observed differences were expected since the Archimedes method is a volume evaluation (3D), in contrast to the image analysis based on the area measurements (2D). Furthermore, the porosity determined by image analysis is influenced by the preparation of the samples and the parameters used for the analysis, such as binarization and segmentation thresholds [43].

Fig. 6 shows microstructures of sintered samples obtained by SEM. The sintered samples revealed different sizes and irregular interconnected pores distributed throughout the microstructure. The microstructures of the 47.5HT-110 MPa and 13.6H-110 MPa samples (Fig. 6, a) and b)) show lower porosity than the other samples. These results were expected based on relative density analysis. On the other hand, the 25HT-65 MPa and 7.1H-65 MPa samples (Fig. 6, c) and d)) had higher pores. When comparing samples sintered at 17.5HT-50 MPa and 5H-50 MPa (Fig. 6, e) and f)), an increase in pore size and different morphologies of the pores can be observed, ranging from irregular to spherical. Therefore, the increased applied pressure and pressure rate improved the densification, morphology, and connectivity of the pores.

Table 3 – Crystallite size and microstrain ($<\varepsilon^2>^{1/2}$) obtained from the Williamson-Hall method for the sintered samples.

Samples	Crystallite Size (nm)	$<\varepsilon^2>^{1/2}*10^{-3}$
47.5HT-110 MPa	34.165 ± 0.008	1.528 ± 0.008
13.6H-110 MPa	50.967 ± 0.014	0.896 ± 0.014
25HT-65 MPa	65.232 ± 0.010	0.766 ± 0.010
7.1H-65 MPa	71.875 ± 0.004	0.522 ± 0.004
17.5HT-50 MPa	73.700 ± 0.007	0.539 ± 0.007
5H-50 MPa	75.533 ± 0.008	0.478 ± 0.008

Fig. 7 provides a better understanding of the effect of pressure on the number (volume fraction), size (S_p), and circularity of pores (C_i) on sintered samples. As expected, pressure reduced the number of large pores, as discussed above. Regarding the analysis of the pore size distribution, a trend of a higher percentage of pores smaller than 10 μm was observed for the case of the samples sintered at 110 MPa, mainly for the 47.5HT-110 MPa sample. For samples sintered at 50 MPa, a larger size and volume fraction of the pores, as well as a higher number of isolated pores were observed. The shift towards smaller pore sizes occurred mainly in the range of 3–15 μm (Fig. 6, a)) as found in other works [14,27,44].

In addition, Fig. 7 a) displays pore size frequency distribution and b) displays the circularity. Only 52% of the measured pores present a circularity index greater than 0.67. Concluding, the different routes of pressures applied during the holding time and heating were selected based on previous studies to induce a variation and comparison between the morphology and pore sizes; thanks to the versatility of the SPS and high pressures could significantly decrease pore volume fraction, which agrees with density results, as shown in the literature [21,25,44].

3.2.3. *Grain size*

Fig. 8 shows the microstructures of samples after sintering. The average grain size and their standard deviation are displayed in Table 5. The increase in pressure reduces the average grain size as expected. The crystallite size analysis corroborates this result described previously in Table 4. It is worth mentioning that pressure is the most striking factor in controlling grain growth during sintering. Studies have addressed the variation of sintered copper grain sizes using SPS following the second route (H), in which the pressure is kept constant during holding time [17,29]. The increase in pressure during holding time probably helped to reduce particle agglomeration due to plastic deformation at the sintering temperature (650°C) [45]. When comparing the 47.5HT-110 MPa sample with the 5H-50 MPa sample, abnormal grain growth can be observed (red circle) in the sample 5H-50 MPa. However, a nonhomogeneous particle agglomeration joined to plastic deformation would have favored grain growth occurrence. Complementary techniques were required to evaluate this result. Statistical evaluation was carried out based on analysis of variance (ANOVA).

3.3. *Statistical analysis*

Table 6 shows the ANOVA results to assess the statistical significance of the grain size distribution under different applied pressures and different sintering routes.

In addition, Tukey (T) test comparisons were carried out to confirm where the differences occurred. Analyses were performed to investigate whether the differences between the average between the two data sets were significantly different. This analysis helps to determine if there is a relationship between Factor A (maximum pressure reached in MPa) and Factor B (rate pressure on HT and H routes), considering the level of significance of 5%, as used in previous studies [46–48].

Table 4 – Density of samples sintered.

Samples	Density		
	Density (g/cm^3)	Porosity - Archimedes method (%)[a]	Porosity - image analysis (%)
47.5HT-110 MPa	8.78	2.0 ± 0.5	1.4 ± 0.4
13.6H-110 MPa	8.60	3.5 ± 0.9	2.5 ± 0.6
25HT-65 MPa	8.15	9.0 ± 0.8	4.1 ± 1.2
7.1H-65 MPa	7.88	12.0 ± 1.7	6.8 ± 1.9
17.5HT-50 MPa	7.71	14.0 ± 1.1	9.0 ± 1.8
5H-50 MPa	7.17	20.0 ± 0.7	13.0 ± 1.3

[a] Copper density = 8.96 g/cm^3 [38].

Prior results (Table 5) suggested that the increase in the sintering pressure caused a decrease in the average grain sizes of the samples. The results based on ANOVA One Way (Table 6) indicated statistically significant differences related to the factors A and B, and their interaction since $p < 0.05$ for all these cases.

According to Tuckey's test, shown in Table 7, focusing on Factor A – sintering pressure, the average grain size of the

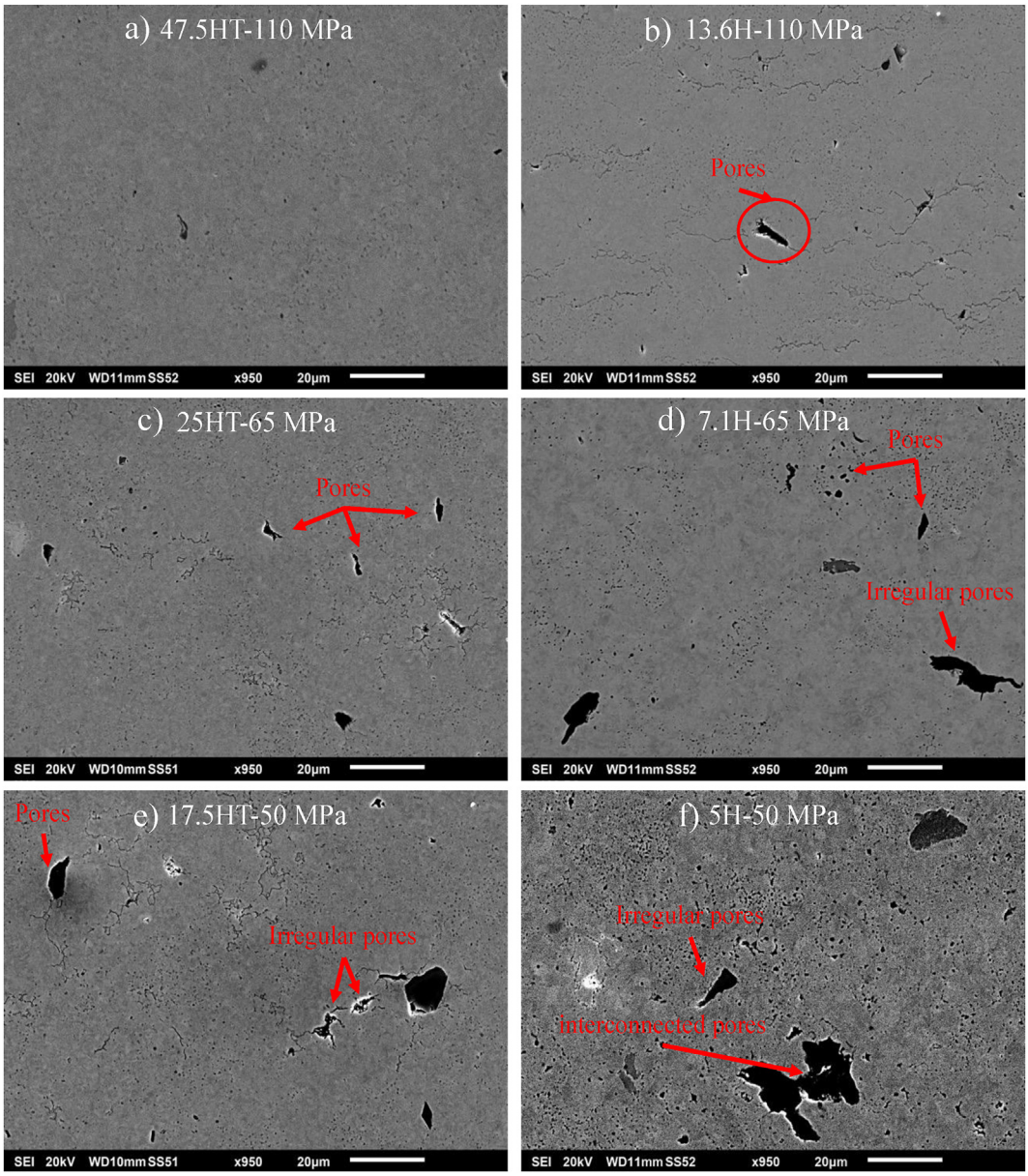

Fig. 6 – SEM images of the morphology and pore sizes for each synthesized copper sample.

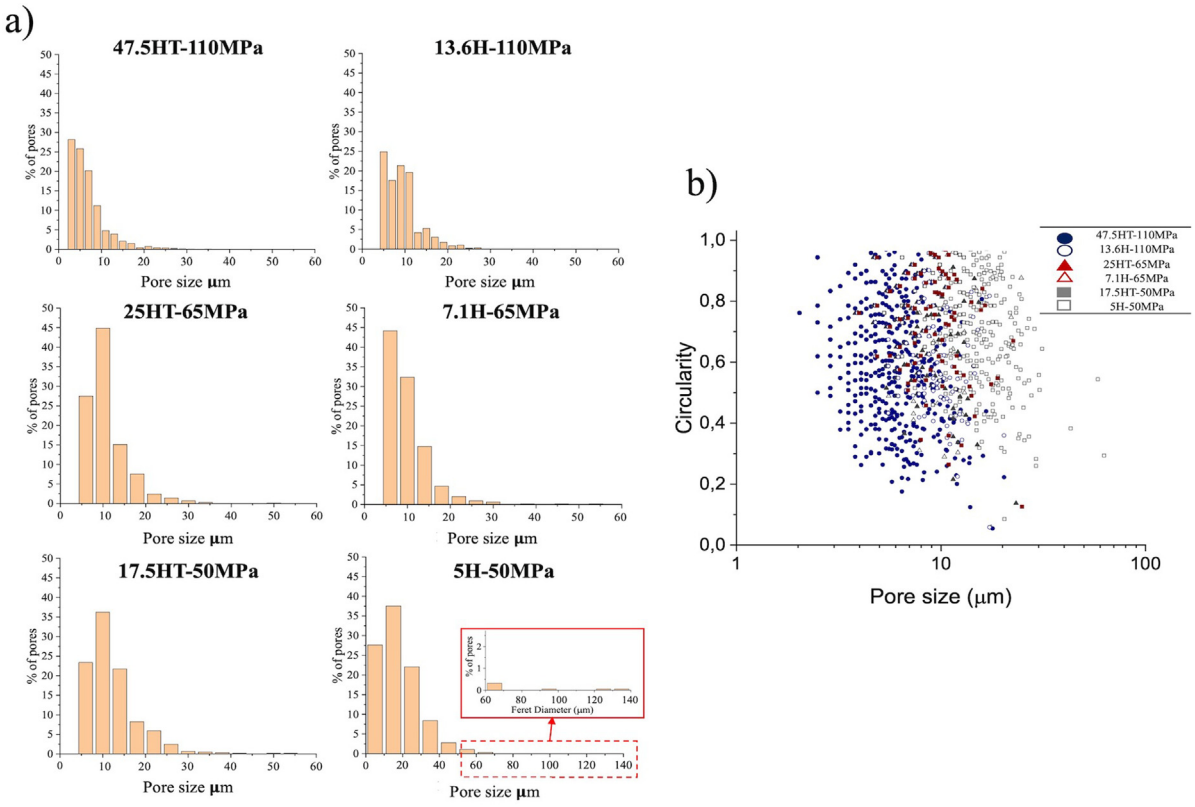

Fig. 7 – (a) Histogram of the pore size and (b) Histogram of the circularity index pores for the sintered materials.

sintered samples was not statistically different between the pressure routes only for the case of 110 MPa. Although, there was a statistical difference between the pressure routes considering the 65 and 50 MPa because the $T_{0.05}$ obtained for this pairwise test was 0.33, which is less than the difference between the averages. Therefore, for a higher significance level, all sintered samples might present a statistically significant different performance between these routes.

Additionally, Tukey tests were performed in pairs between pressure routes (Factor B). Two cases can be detached in this approach in Table 7: the average grain sizes of the sintered samples cannot be statiscally different at pressure rate during heating (H) and holding time (HT), constrating 65 with 50 MPa.

Considering that the sintering pressure routes can cause changes in the average grain size of the copper samples for the other studied conditions, the following evaluations are summarized based on Tables 6 and 7 in addition to microsctructural characterizations.

- For the two samples sintered at high pressures (110 MPa), no significant changes in the average grain sizes. However, the different routes caused effects in pore sizes (see Fig. 6). When the first route (HT) and the second route (H) are compared for 110 vs. 65 MPa and 110 vs. 50 MPa of sintering pressure, a significant difference between the average grain sizes is found (Table 7). In addition, change in porosity can be observed (see porosity Figs. 7 and 8).
- Regardless of how the pressure is applied, the increase in pressure causes a decrease in the average grain size. Nevertheless, the 47.5HT-110 MPa sample has shown a better performance between lower porosity and grain size. Consequently, an optimization of the sintering parameters of the sintered copper via SPS has been obtained.

3.4. *Hardness*

Table 8 presents the mean values and standard deviation of Vickers hardness. The microhardness was preliminary evaluated at different loads, and an increase in Vickers hardness at lower loads was observed expected (Meyers law); moreover, the porosity distribution and size present heterogeneities, mainly in the low-density samples. Therefore, the selected load was 10 gf since comparable results were obtained, and the heterogeneity of samples would be evaluated based on standard deviation.

Vickers hardness measurements indicate that the different routes of sintering pressures of 110 MPa influence the hardness, which is consistent with the variation in crystallite size, microstrain, density, and grain size. The 47.5HT-110 MPa sample presented the highest hardness, similar to that found in nanometric copper powder and the manufacture of sintered copper composites by SPS [19,20]. Moreover, an increase in hardness is expected with decreasing porosity [48]. Microhardness can be closely related to the resistance of the

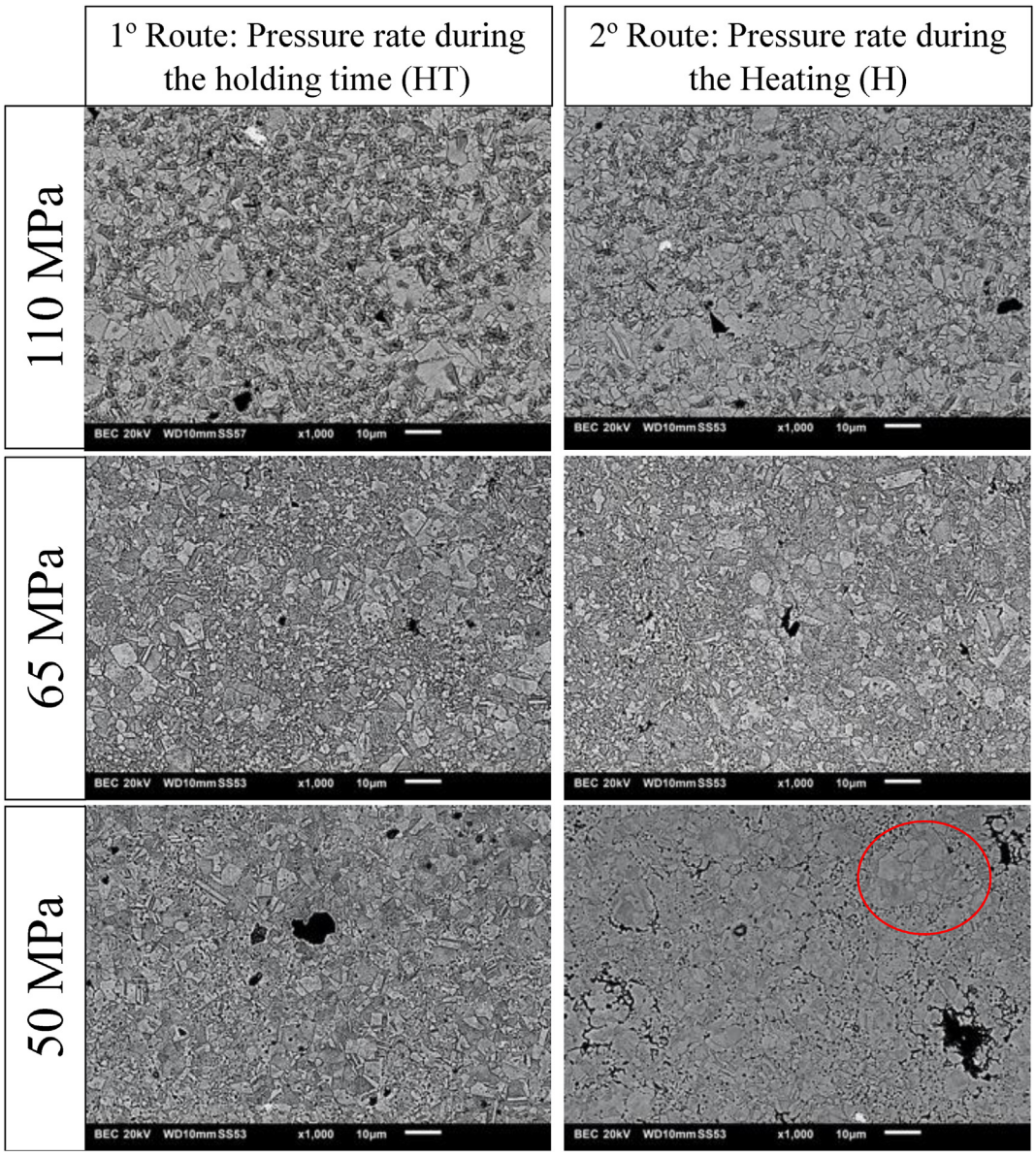

Fig. 8 – SEM micrographs (backscattered electrons) - Microstructure of the sintered samples.

material under plastic deformation to penetration during normal external compressive force, as described by Tabor [49] and Carsley et al. [50]. The decrease in grain size influences an increase in yield strength, as demonstrated in the Hall-Petch relationship [19,51].

Table 5 – The average grain size of each sintered sample.

Samples	Average Grain Size (µm)
47.5HT-110 MPa	3.1 ± 0.8
13.6H-110 MPa	3.3 ± 1.0
25HT-65 MPa	4.2 ± 1.0
7.1H-65 MPa	4.8 ± 1.2
17.5HT-50 MPa	4.5 ± 1.2
5H-50 MPa	5.3 ± 1.0

3.4.1. *Mean free path*

The mean free path between pores (λ) is a measure of the spatial distribution of the pores, defined as the mean distance between the limits of the pores, equation (3) [52].

$$\lambda = d\left(\frac{1 - V_{vp}}{V_{vp}}\right) \quad (3)$$

where d is the mean pore diameter and V_{vp} is the total volume fraction of porosity.

The mean free path can be used to relate the effects of the microstructure, density and hardness of sintered samples. Table 9 shows the mean free path between the pores in the sintered samples. As the pressure increases, the mean free path increases due to the increased distance between pores and a decrease in pore size, as observed in Figs. 6 and 7. The sintered samples, with pressures of 50 MPa, had a mean free

Table 6 – ANOVA tests (p = 5% significance level) of the grain size of the samples sintered.

Factor A	Factor B
50	Pressure rate during holding time (HT)
	Pressure rate during heating (H)
65	Pressure rate during holding time (HT)
	Pressure rate during heating (H)
110	Pressure rate during holding time (HT)
	Pressure rate during heating (H)

ANOVA Grain Size

Source of variation	Sum of Squares	Degree of Freedom	Mean Square	F_o	P_value
Factor A	397.9	2	198.9	47.1	0.0
Factor B	211.0	1	211.0	50.0	$2.22e^{-12}$
Interaction	317.3	2	158.7	37.6	$1.11e^{-16}$
Error	7342.6	1740	4.2		
Total	8268.8	1745			

path lower due to a higher fraction of pores, as a trend exhibited in Table 4 and Fig. 6. Therefore, there is a directly proportional relationship between hardness (Table 8) and the mean free path between the pore volume fraction, where an increase in the mean free path leads to an increase in hardness. The sample sintered at 47.5HT-110 MPa is expected to have optimal mechanical properties.

3.5. *Finite element approach - effect of different sintering pressure routes*

The results of the numerical simulation of the stress distribution (in the plane x-y) on the upper surface of the samples, regarding the effect of the axial pressure application process during the sintering process of 25HT-65 MPa and 7.1H-65 MPa samples are presented in Fig. 9. A pressure of 65 MPa was selected since it represents intermediary results but follows the same trend as other results.

Results of 25HT-65 MPa sample stress simulation shows a stress rise (red areas) during the sintering, considering the difference between 420 e 540 s. This increase in tensile stresses is due to a high rate of applied pressure, starting with a pressure of 15 MPa at 420 s reaching a maximum pressure of 65 MPa at 540 s at the moment that sintering ends. Comparatively, 7.1H-65 MPa sample simulations indicated higher stress (red areas) concentrations than the 25HT-65 MPa sample at a time of 420 s. Higher stresses occur because, at 420 s, the sintering pressure has already reached the maximum pressure.

Another relevant result is obtained comparing the compressive stress given in the first and second route pressures; the following results were verified: (i) 420 s condition (after heating) - an area filled by the compressive state on the first route sample (25HT-65 MPa) reached about of 7,5% more than the second route sample (7.1H-65 MPa); i.e., the first one tends to provide the best mechanical response at this step; and (ii) 540 s condition (after holding time) – the compressive stress area was about of 1,0% higher for the first route sample, consolidating its enhanced mechanical behavior.

Although the two samples present similar stress distributions at 540 s, changes in porosity were also experimentally observed (Table 4 and Fig. 6) following the literature [53]. This

Table 7 – Pairwise comparisons of grain sizes (Factor A and Factor B) based on Tukey's test after ANOVA analysis.

Tukey		Subtraction between average grain sizes	Statistically significant?
Factor B	$T_{0.05}$ (3.32)		
H			
13.6H-110 MPa v/s 7.1H-65 MPa	0.399	1.51	Yes
13.6H-110 MPa v/s 5H-50 MPa	0.399	2.00	Yes
7.1H-65 MPa v/s 5H-50 MPa	0.399	0.37	No
HT			
47.5HT-110 MPa v/s 25HT-65 MPa	0.399	1.06	Yes
47.5HT-110 MPa v/s 17.5HT-50 MPa	0.399	1.45	Yes
25HT-65 MPa v/s 17.5HT-50 MPa	0.399	0.39	No
Factor A	$T_{0.05}$ (2.77)		
110 MPa			
47.5HT-110 MPa v/s 13.6H-110 MPa	0.333	0.23	No
65 MPa			
25HT-65MPa v/s 7.1H-65 MPa	0.333	0.68	Yes
50 MPa			
17.5HT-50MPa v/s 5H-50 MPa	0.333	0.78	Yes

Table 8 – Vickers microhardness of samples sintered.

Samples	$HV_{0.01}$
47.5HT-110 MPa	108.0 ± 5.7
13.6H-110 MPa	95.4 ± 12.2
25HT-65 MPa	84.9 ± 5.3
7.1H-65 MPa	88.9 ± 13.1
17.5HT-50 MPa	78.2 ± 32.6
5H-50 MPa	75.9 ± 8.3

Table 9 – Variation of the Mean free path between pores (λ) of samples sintered.

Samples	Mean free path between pores (μm)
47.5HT-110 MPa	31.1 ± 2.2
13.6H-110 MPa	21.4 ± 3.0
25HT-65 MPa	10.5 ± 4.5
7.1H-65 MPa	9.4 ± 4.4
17.5HT-50 MPa	7.3 ± 5.6
5H-50 MPa	7.6 ± 5.0

influence can be related to the thermal effects responsible for an increase in the ductility of the copper and the magnitude of the applied pressure. Additionally, the elastic limit of copper decreases with increasing temperature, as reported in the literature [54,55]. Therefore, once the applied stress reaches the elastic limit of the material at 650 °C, densification will proceed through plastic deformation under a pressure of 65 MPa or a pressure rate of 25 MPa min^{-1}. Such instantaneous deformation is independent of time and can be considered a rapid densification mechanism [56]. Therefore, maintaining a constant pressure during holding time (HT) or heating (H) can cause a difference in plastic deformation during the holding time step. In addition, the simulation can corroborate the differences between the experimental pressure routes studied.

3.6. *Effect of pressure and pressure routes*

The powder is usually pressed before the sintering in the conventional sintering process. A near-net shape material is obtained and subsequently sintered. SPS is a pressure-assisted process; hence the pressure is applied during the sintering, which causes the deformation of ductile powder. Moreover, gases are expelled from pore regions. As a result, there is an increase in the driving force for densification in addition to a decrease in the surface energy due to boundary and interface area reduction [57]. Therefore, pressure assisted system of SPS allows high densification at temperatures lower than conventional sintering. For instance, the conventional copper sintering temperature is around 1000°C, and in this study, 650 °C and 110 MPa of pressure were enough to obtain about 98% of the density.

Regarding the effect of pressure, the increase in pressure led to an improvement in the densification and, consequently, less volume fraction of pores, smaller grain size, smaller crystallite size, higher microstrain, and higher hardness. All of the results are reinforced based on the microstrain and hardness, which indicate an increase in crystalline defects

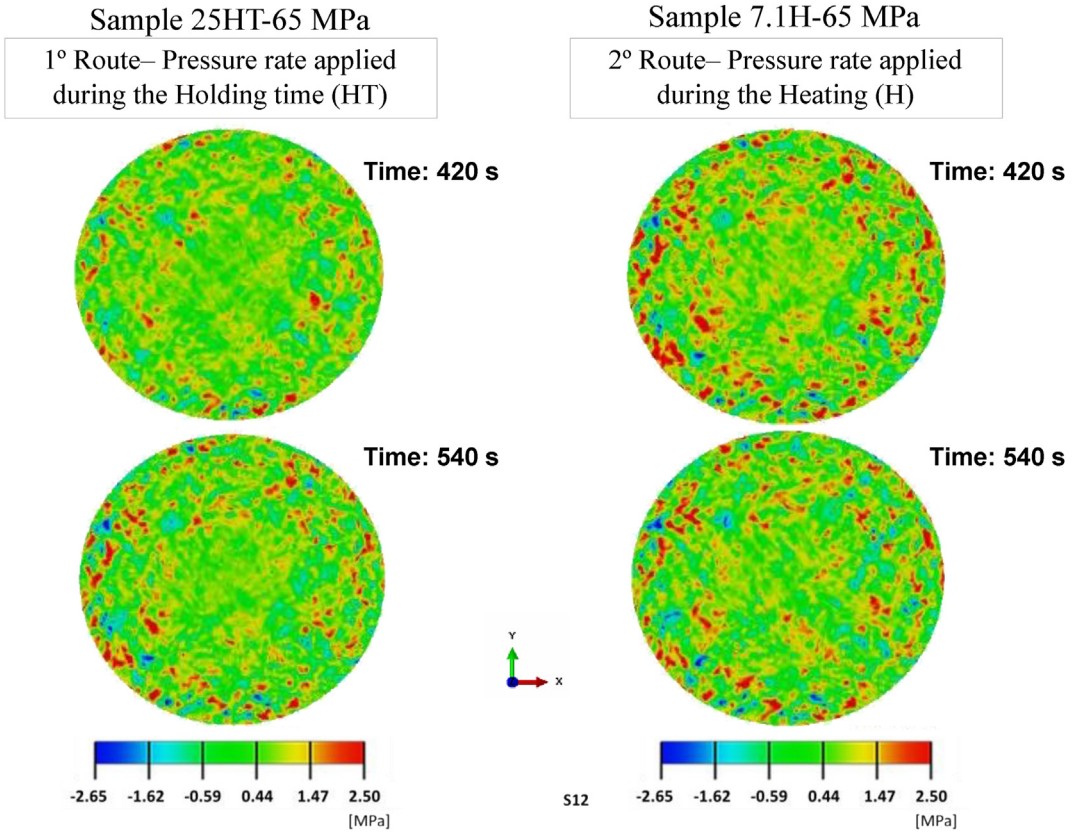

Fig. 9 – Distribution of stresses (x-y plane) in 25HT-65 MPa and 7.1H-65 MPa samples during the holding time process (420 and 540 s).

due to deformation. Thus, the balance of decrease in the surface energy and deformation is observed in the obtained results.

The other aspect is the pressure route used. The pressure increase during the holding time was pronounced in densification, grain size, crystallite size, pore volume fraction, and hardness, mainly in the microstrain. The results of microstrain in the sample 47.5HT-110 MPa and 25HT-65 MPa show an increase in crystalline defects that were corroborated by numerical simulation results. Although other experimental techniques, such as transmission electron microscopy, be necessary to prove the hypothesis made, a constant pressure during holding time (HT) or heating (H) can cause a difference in plastic deformation and densification will be improved by plastic deformation once the stress reaches the elastic limit at 650 °C. The densification is rate-independent at stress levels above the temperature-compensated yield stresses. As the pressure levels diminish with higher density and grain growth, the pressure effects become dominated by rate-dependent creep and/or diffusion mechanisms [57].

4. Conclusions

The main contribution of this study consisted of evaluating the SPS pressure-assisted system parameters on copper densification and microstructural evolution. The microstructural and mechanical characterization showed that the pressure and the route of applied pressure during heating or holding time influenced the densification. The higher the maximum pressure, the higher the densification and mechanical properties. The best results were found in samples sintered at 110 MPa Moreover, the pressure applied during the holding time (first route), in which the Cu was at 650 °C, showed the best results. FEM analysis confirmed higher compressive stress conditions on the first route, which agrees with experimental findings.

The conducted analysis allowed to highlight the following conclusions.

(1) Microstructure: densities of the sintered samples are found to rise with the sintering pressure increase, and an almost total density of 97.5% was obtained using the first route (HT), un which the pressure was applied during holding time at a pressure of 110 MPa. Also, grain sizes were characterized in the range of approximately 3.0–5.5 μm. Comparing the threshold sintering parameters of 50 MPa (second route – H) and 110 MPa (first route - HT), growth inhibition of 58% was observed, indicating a range of grain size and porosities can be designed using the SPS technique.
(2) The crystallite size and microstrain measurements indicated that the highest pressure applied (110 MPa) during the SPS process resulted in a decrease in crystallite size. Otherwise, increasing the pressure provides higher microstrain values. The results of microstrain indicates the plastic deformation occurred during holding time improve the densification. In addition, FEM analysis corroborates the findings since the stress state of the samples based on the thermomechanical loadings during sintering are more compressive in the HT route, increasing the applied pressure during holding time.
(3) Vickers microhardness values of the sintered samples depended on the sintering route and pressure as the microstructural features. Higher pressures significantly affected the hardness improvement, which can be assigned to the lower grain size and porosity.

Data availability

The raw data required to reproduce these findings are available and can be used prior authorization from the authors. Contact francisco.briones@pucv.cl for more information.

Declaration of competing interest

The authors declare that they have no known competing financial interests or personal relationships that could have appeared to influence the work reported in this paper.

Acknowledgments

The authors acknowledge the support of the Brazilian funding agencies CNPq, CAPES, FAPESP Nº 2020/10653-5 and Chile's funding agency ANID Becas-Chile Ph.D. student.

REFERENCES

[1] Kovalchenko AM, Fushchich OI, Danyluk S. The tribological properties and mechanism of wear of Cu-based sintered powder materials containing molybdenum disulfide and molybdenum diselenite under unlubricated sliding against copper. Wear 2012. https://doi.org/10.1016/j.wear.2012.05.001.
[2] Xiao Y, Zhang Z, Yao P, Fan K, Zhou H, Gong T, et al. Mechanical and tribological behaviors of copper metal matrix composites for brake pads used in high-speed trains. Tribol Int 2018. https://doi.org/10.1016/j.triboint.2017.11.038.
[3] Bares JA, Argibay N, Mauntler N, Dudder GJ, Perry SS, Bourne GR, et al. High current density copper-on-copper sliding electrical contacts at low sliding velocities. Wear 2009. https://doi.org/10.1016/j.wear.2008.12.062.
[4] Ramirez DA, Murr LE, Martinez E, Hernandez DH, Martinez JL, MacHado BI, et al. Novel precipitate-microstructural architecture developed in the fabrication of solid copper components by additive manufacturing using electron beam melting. Acta Mater 2011. https://doi.org/10.1016/j.actamat.2011.03.033.
[5] Felege GN, Gurao NP, Upadhyaya A. Microstructure, microtexture and grain boundary character evolution in microwave sintered copper. Mater Char 2019. https://doi.org/10.1016/j.matchar.2019.109921.
[6] Dixit M, Srivastava RK. Effect of compaction pressure on microstructure, density and hardness of Copper prepared by Powder Metallurgy route. IOP Conf Ser Mater Sci Eng 2018. https://doi.org/10.1088/1757-899X/377/1/012209.

[7] Xiao JK, Zhang W, Zhang C. Microstructure evolution and tribological performance of Cu-WS2 self-lubricating composites. Wear 2018. https://doi.org/10.1016/j.wear.2018.07.024.
[8] Pan Y, Xiao SQ, Lu X, Zhou C, Li Y, Liu ZW, et al. Fabrication, mechanical properties and electrical conductivity of Al2O3 reinforced Cu/CNTs composites. J Alloys Compd 2019;782:1015–23. https://doi.org/10.1016/j.jallcom.2018.12.222.
[9] Romaric C, Sophie LG, Foad N, Frédéric C, Guillaume B, Gilbert F, et al. Effect of current on the sintering of pre-oxidized copper powders by SPS. J Alloys Compd 2017;692:478–84. https://doi.org/10.1016/j.jallcom.2016.08.191.
[10] Lee G, Manière C, McKittrick J, Olevsky EA. Electric current effects in spark plasma sintering: from the evidence of physical phenomenon to constitutive equation formulation. Scripta Mater 2019;170:90–4. https://doi.org/10.1016/j.scriptamat.2019.05.040.
[11] Antou G, Guyot P, Pradeilles N, Vandenhende M, Maître A. Identification of densification mechanisms of pressure-assisted sintering: application to hot pressing and spark plasma sintering of alumina. J Mater Sci 2015;50:2327–36. https://doi.org/10.1007/s10853-014-8804-0.
[12] Machado IF, Boidi G, Fukumasu NK, Tertuliano AJO, Seriacopi V, Souza RM. Effect of sintering densification on micro-scale mechanical and tribological behaviour of niobium carbide. Wear 2021;482–483:203958. https://doi.org/10.1016/j.wear.2021.203958.
[13] Cheng Y, Cui Z, Cheng L, Gong D, Wang W. Effect of particle size on densification of pure magnesium during spark plasma sintering. Adv Powder Technol 2017;28:1129–35. https://doi.org/10.1016/j.apt.2017.01.017.
[14] Diouf S, Molinari A. Densification mechanisms in spark plasma sintering: effect of particle size and pressure. Powder Technol 2012;221:220–7. https://doi.org/10.1016/j.powtec.2012.01.005.
[15] Borkar T, Banerjee R. Influence of spark plasma sintering (SPS) processing parameters on microstructure and mechanical properties of nickel. Mater Sci Eng 2014;618:176–81. https://doi.org/10.1016/j.msea.2014.08.070.
[16] Babapoor A, Asl MS, Ahmadi Z, Namini AS. Effects of spark plasma sintering temperature on densification, hardness and thermal conductivity of titanium carbide. Ceram Int 2018;44:14541–6. https://doi.org/10.1016/j.ceramint.2018.05.071.
[17] Zhaohui Z, Fuchi W, Lin W, Shukui L, Osamu S. Sintering mechanism of large-scale ultrafine-grained copper prepared by SPS method. Mater Lett 2008;62:3987–90. https://doi.org/10.1016/j.matlet.2008.05.036.
[18] Zhang ZH, Wang FC, Wang L, Li SK, Shen MW, Osamu S. Microstructural characteristics of large-scale ultrafine-grained copper. Mater Char 2008. https://doi.org/10.1016/j.matchar.2007.06.014.
[19] Ritasalo R, Cura ME, Liu XW, Söderberg O, Ritvonen T, Hannula SP. Spark plasma sintering of submicron-sized Cu-powder-Influence of processing parameters and powder oxidization on microstructure and mechanical properties. Mater Sci Eng 2010;527:2733–7. https://doi.org/10.1016/j.msea.2010.01.008.
[20] Zhu KN, Godfrey A, Hansen N, Zhang XD. Microstructure and mechanical strength of near- and sub-micrometre grain size copper prepared by spark plasma sintering. Mater Des 2017. https://doi.org/10.1016/j.matdes.2016.12.042.
[21] Wegner M, Leuthold J, Peterlechner M, Setman D, Zehetbauer M, Pippan R, et al. Percolating porosity in ultrafine grained copper processed by High Pressure Torsion. J Appl Phys 2013;114. https://doi.org/10.1063/1.4829705.
[22] Wang SW, Chen LD, Kang YS, Niino M, Hirai T. Effect of plasma activated sintering (PAS) parameters on densification of copper powder. Mater Res Bull 2000;35:619–28. https://doi.org/10.1016/S0025-5408(00)00246-4.
[23] Zhang ZH, Wang FC, Wang L, Li SK. Ultrafine-grained copper prepared by spark plasma sintering process. Mater Sci Eng, A 2008. https://doi.org/10.1016/j.msea.2007.04.107.
[24] Hu ZY, Zhang ZH, Cheng XW, Wang FC, Zhang YF, Li SL. A review of multi-physical fields induced phenomena and effects in spark plasma sintering: fundamentals and applications. Mater Des 2020. https://doi.org/10.1016/j.matdes.2020.108662.
[25] Knaislová A, Novák P, Cygan S, Jaworska L, Cabibbo M. High-pressure spark plasma sintering (HP SPS): a promising and reliable method for preparing Ti-Al-Si alloys. Materials 2017;10:6–13. https://doi.org/10.3390/ma10050465.
[26] Ghanizadeh S, Grasso S, Ramanujam P, Vaidhyanathan B, Binner J, Brown P, et al. Improved transparency and hardness in α-alumina ceramics fabricated by high-pressure SPS of nanopowders. Ceram Int 2017;43:275–81. https://doi.org/10.1016/j.ceramint.2016.09.150.
[27] Li W, Olevsky EA, McKittrick J, Maximenko AL, German RM. Densification mechanisms of spark plasma sintering: multi-step pressure dilatometry. J Mater Sci 2012;47:7036–46. https://doi.org/10.1007/s10853-012-6515-y.
[28] Dutkiewicz J, Ozga P, Maziarz W, Pstruś J, Kania B, Bobrowski P, et al. Microstructure and properties of bulk copper matrix composites strengthened with various kinds of graphene nanoplatelets. Mater Sci Eng 2015;628:124–34. https://doi.org/10.1016/j.msea.2015.01.018.
[29] Zhang ZH, Wang FC, Lee SK, Liu Y, Cheng JW, Liang Y. Microstructure characteristic, mechanical properties and sintering mechanism of nanocrystalline copper obtained by SPS process. Mater Sci Eng, A 2009. https://doi.org/10.1016/j.msea.2009.07.016.
[30] Bazarnik P, Nosewicz S, Romelczyk-Baishya B, Chmielewski M, Strojny Nędza A, Maj J, et al. Effect of spark plasma sintering and high-pressure torsion on the microstructural and mechanical properties of a Cu–SiC composite. Mater Sci Eng, A 2019. https://doi.org/10.1016/j.msea.2019.138350.
[31] Zhang ZH, Wang FC, Wang L, Li SK, Shen MW, Osamu S. Microstructural characteristics of large-scale ultrafine-grained copper. Mater Char 2008;59:329–33. https://doi.org/10.1016/j.matchar.2007.06.014.
[32] ASTM, ASTM. B962-17 - standard test methods for density of compacted or sintered powder metallurgy (PM) products using Archimedes' principle. 2013. https://doi.org/10.1520/B0962-13.2. West Conshohocken, PA.
[33] Bagheri GH, Bonadonna C, Manzella I, Vonlanthen P. On the characterization of size and shape of irregular particles. Powder Technol 2015;270:141–53. https://doi.org/10.1016/j.powtec.2014.10.015.
[34] Boidi G, Fukumasu NK, Machado IF. Wear and friction performance under lubricated reciprocating tests of steel powder mixtures sintered by Spark Plasma Sintering. Tribol Int 2018. https://doi.org/10.1016/j.triboint.2018.01.032.
[35] ASTM-E92. Standard test method for Vickers hardness of metallic materials. ASTM Int.; 1997.
[36] Williamson GK, Hall WH. X-ray line broadening from filed aluminium and wolfram. Acta Metall 1953;1:22–31. https://doi.org/10.1016/0001-6160(53)90006-6.
[37] Seriacopi V, Fukumasu NK, Souza RM, Machado IF. Finite element analysis of the effects of thermo-mechanical loadings on a tool steel microstructure. Eng Fail Anal 2019;97:383–98. https://doi.org/10.1016/j.engfailanal.2019.01.006.

[38] Williams ML. CRC handbook of chemistry and physics. 76th edition Occup Environ Med 1996;53:504. https://doi.org/10.1136/oem.53.7.504. 504.
[39] Friel JJ, Grande JC, Hetzner D, Kurzydlowski K, Laferty D, Shehata MT, et al. Practical guide to image analysis. Washington DC: ASM International; 2000.
[40] Volume 2 ASM International. Volume 2 properties and selection: nonferrous alloys and special-purpose materials. ASM, Int. 1990;2:583–8. https://doi.org/10.1007/s004310050884.
[41] Ross RB. Materials specification handbook metallic materials specification handbook. fourth ed. 2013.
[42] Martínez C, Briones F, Aguilar C, Araya N, Iturriza I, Machado I, et al. Effect of hot pressing and hot isostatic pressing on the microstructure, hardness, and wear behavior of nickel. Mater Lett 2020. https://doi.org/10.1016/j.matlet.2020.127944.
[43] Shahedi Asl M, Ahmadi Z, Parvizi S, Balak Z, Farahbakhsh I. Contribution of SiC particle size and spark plasma sintering conditions on grain growth and hardness of TiB2 composites. Ceram Int 2017;43:13924–31. https://doi.org/10.1016/j.ceramint.2017.07.121.
[44] Makena MI, Shongwe MB, Ramakokovhu MM, Olubambi PA. Effect of sintering parameters on densification, corrosion and wear behaviour of Ni-50Fe alloy prepared by spark plasma sintering. J Alloys Compd 2017;699:1166–79. https://doi.org/10.1016/j.jallcom.2016.12.368.
[45] Quach DV, Avila-Paredes H, Kim S, Martin M, Munir ZA. Pressure effects and grain growth kinetics in the consolidation of nanostructured fully stabilized zirconia by pulsed electric current sintering. Acta Mater 2010;58:5022–30. https://doi.org/10.1016/j.actamat.2010.05.038.
[46] Chávez-Vásconez R, Lascano S, Sauceda S, Reyes-Valenzuela M, Salvo C, Mangalaraja RV, et al. Effect of the processing parameters on the porosity and mechanical behavior of titanium samples with bimodal microstructure produced via hot pressing. Materials 2022;15. https://doi.org/10.3390/ma15010136.
[47] Ribeiro YD, Soares AC, Oliveira MP, de Oliveira BF, Pereira AC, Monteiro SN. Development and characterization of spark plasma sintered novel Ni, Cu, WC containing Nb-Based alloys for high-temperature applications. J Mater Res Technol 2022;17:789–801. https://doi.org/10.1016/j.jmrt.2022.01.030.
[48] Jana P, Ray S, Goldar D, Kota N, Kar SK, Roy S. Study of the elastic properties of porous copper fabricated via the lost carbonate sintering process. Mater Sci Eng 2022;836:142713. https://doi.org/10.1016/j.msea.2022.142713.
[49] TABOR D. The hardness of solids. Rev Phys Technol 1970. https://doi.org/10.1088/0034-6683/1/3/i01.
[50] E.C.A., Carsley JE, Fisher A, Milligan WW. Mechanical behavior of a bulk nanostructured iron alloy. Metall Mater Trans 1998;29:2261–71.
[51] Surekha K, Els-Botes A. Development of high strength, high conductivity copper by friction stir processing. Mater Des 2011;32:911–6. https://doi.org/10.1016/j.matdes.2010.08.028.
[52] de Mello JDB, Binder R, Klein AN, Hutchings IM. Effect of compaction pressure and powder grade on microstructure and hardness of steam oxidised sintered iron. Powder Metall 2001;44:53–61. https://doi.org/10.1179/003258901666176.
[53] Souza RM, Ordoñez MFC, Mezghani S, Crequy S, Fukumasu NK, Machado IF, et al. Orthogonal cut of SPS-sintered composites with ferrous matrix and Fe[sbnd]Mo[sbnd]S particles: numerical and experimental analysis. Tribol Int 2020. https://doi.org/10.1016/j.triboint.2019.04.034.
[54] Yang B, Motz C, Rester M, Dehm G. Yield stress influenced by the ratio of wire diameter to grain size - a competition between the effects of specimen microstructure and dimension in micro-sized polycrystalline copper wires. Philos Mag 2012;92:3243–56. https://doi.org/10.1080/14786435.2012.693215.
[55] Carreker RP, Hibbard WR. Tensile deformation of high-purity copper as a function of temperature, strain rate, and grain size. Acta Metall 1953;1. https://doi.org/10.1016/0001-6160(53)90022-4.
[56] Fang ZZ, Wang H, Kumar V. Coarsening, densification, and grain growth during sintering of nano-sized powders—a perspective. Int J Refract Met Hard Mater 2017;62:110–7. https://doi.org/10.1016/j.ijrmhm.2016.09.004.
[57] Castro Ricardo HR, Gouvêa Douglas. Sintering and nanostability: the thermodynamic perspective. J Am Ceram Soc 2016;99. https://doi.org/10.1111/jace.14176.